Real-Time AFM and Impedance Corrosion Monitoring of Environmentally Friendly Ceria Films on AA7075

Journal of The Electrochemical Society, 2020 **167** 101503

Real-Time AFM and Impedance Corrosion Monitoring of Environmentally Friendly Ceria Films on AA7075

Sanja I. Stevanović,[1] Maria Lekka,[2] Alex Lanzutti,[2] Nikola Tasić,[3] Ljiljana S. Živković,[4] Lorenzo Fedrizzi,[2] and Jelena B. Bajat[5,*,z]

[1]*ICTM-Department of Electrochemistry, University of Belgrade, 1100 Belgrade, Serbia*
[2]*University of Udine, Department of Engineering and Architecture of University of Udine, 33100 Udine, Italy*
[3]*Institute for Multidisciplinary Research, Department of Materials Science, University of Belgrade, 11030 Belgrade, Serbia*
[4]*Department of Chemical Dynamics and Permanent Education, „VINČA' Institute of Nuclear Sciences - National Institute of the Republic of Serbia, University of Belgrade, 11001 Belgrade, Serbia*
[5]*Faculty of Technology and Metallurgy, University of Belgrade, 11120 Belgrade, Serbia*

Cerium-based conversion coatings have emerged as promising green alternatives to the harmful chromium-based ones, but the mechanism of corrosive protection still remains a subject of academic and industrial research. This study focuses at small scale phenomena of corrosion inhibition imparted by ceria (CeO_2) to AA7075. Ceria nanoparticles were deposited from diluted and concentrated CeO_2 sols by immersion. A multi-analytical approach, combining Atomic Force microscopy (AFM), Scanning Kelvin Probe Force Microscopy, Glow Discharge Optical Emission Spectroscopy, open circuit potential and electrochemical impedance spectroscopy was employed. Deposition of ceria films led to deactivation of cathodic sites, i.e. decreased Volta potential difference, resulting in increased corrosion inhibition. In situ AFM real-time monitoring revealed that during exposure to NaCl electrolyte, the changes in size of deposited ceria aggregates occurred: nanoparticles disintegrated/desorbed and re-deposited at the coating surface. The process was found to be dynamic in nature. Small particles size and inherent reactivity are believed to accelerate this phenomenon. Due to the greater CeO_2 reservoir, this phenomenon was more pronounced with a thicker film, imparting longer term protection.

 [DOI: 10.1149/1945-7111/ab98af]

Manuscript submitted April 2, 2020; revised manuscript received May 26, 2020. Published June 11, 2020.

Supplementary material for this article is available online

Conversion coatings based on rare earth elements have emerged as promising ecologically acceptable alternatives to chromate protective coatings.[1–6] Among them, cerium based coatings (cerium oxides/hydroxides) have been researched either as a sole coating or as an inhibitor in the organic or hybrid coatings.[7–12] Starting from the pioneering research on Ce inhibition ability,[13–15] a large variety of solutions were utilized in chemical and physical deposition routes to ceria conversion coatings (CeCC): nitrate,[9,16–20] chloride,[3,4,21–23] spray–drain cycles, magnetron sputtering and chemical vapour deposition were also reported.[24–27] Common features appeared in most methods: substrate de-oxidation/activation, as a necessary pre-treatment step, followed by CeCCs formation, proceeding via several successive steps.

All aluminium alloys have some type of intermetallic particles (IMPs), varying upon the chemical content and processing technique, mostly heat-treatment. AA-7075 has a very heterogeneous structure, containing many different intermetallic particles.[28–31] Depending on the nature, the IMPs could be either cathodic, with more noble potential relative to matrix, promoting the matrix dissolution (Cu and Fe-containing ones) or anodic, that are active and dissolve preferentially, due to the negative potential in respect to the matrix (Mg-rich intermetallics). Some of the typical IMPs in AA7075 are: Al_7Cu_2Fe, Al_2CuFe, Al_2CuMg, Al_2Cu, Al_2CuMg, Al_3Fe and Mg_2Si. This alloy type also contains strengthening $MgZn_2$ particles (η-phase), dispersed throughout the alloy matrix.

According to the mechanism of Al dissolution and pit formation, proposed by Park et al.,[32] the Al matrix corrosion in aluminium alloys is initiated due to the galvanic coupling established between Al matrix and some of the constituent alloy intermetallic particles (IMPs), that facilitate oxygen reduction. So, this cathodic reaction takes place mainly at IMPs (Eq. 1), while the anodic counterpart reaction is matrix dissolution (Eq. 2).

$$O_2 + 2H_2O + 4e^- \rightarrow 4OH^- \quad [1]$$

$$Al \rightarrow Al^{3+} + 3e^- \quad [2]$$

The generated OH^- ions facilitate a deposition of cerium hydroxide (Eqs. 3 and 4) and further their dehydration leads to cerium oxide (ceria) formation (Eqs. 5–8)[14,15,33]:

$$Ce^{3+} + 3OH^- \rightarrow Ce(OH)_3 \quad [3]$$

$$4Ce^{3+} + O_2 + 4OH^- + 2H_2O \rightarrow 4Ce(OH)_2{}^{2+} \quad [4]$$

$$Ce(OH)_3 \rightarrow CeO_2 + H_3O^+ + e^- \quad [5]$$

$$Ce(OH)_2{}^{2+} + 2OH^- \rightarrow CeO_2 + 2H_2O \quad [6]$$

$$Ce(OH)_2{}^{2+} + 2OH^- \rightarrow Ce(OH)_4 \quad [7]$$

$$Ce(OH)_4 \rightarrow CeO_2 \cdot 2H_2O \quad [8]$$

It is widely accepted nowadays that the ceria coating thus produced (as hydrated cerium oxide) retards the cathodic reaction, thereby reducing the corrosion rate of substrate.[4,9,23,25,26,33]

The literature reports on the deposition of the ceria coatings were mainly based on utilizing nitrates or chlorides as the Ce source. Our idea was to deposit the ceria coating starting from the colloidal dispersion of ceria nanoparticles (sol) and to avoid, in such a manner, the usual pH-driven process (Eqs. 1–8). Moreover, since the used sol was laboratory prepared and of a low pH, there was no need for the aluminium alloy activation as a common step in ceria deposition, making this procedure convenient as a single step one.

A complete insight of the protection mechanisms provided by cerium oxide nanoparticles still remains a challenge. Only a few studies dealt with synthesis of the ceria sol[34–36] and its application as

*Electrochemical Society Member.
[z]E-mail: jela@tmf.bg.ac.rs

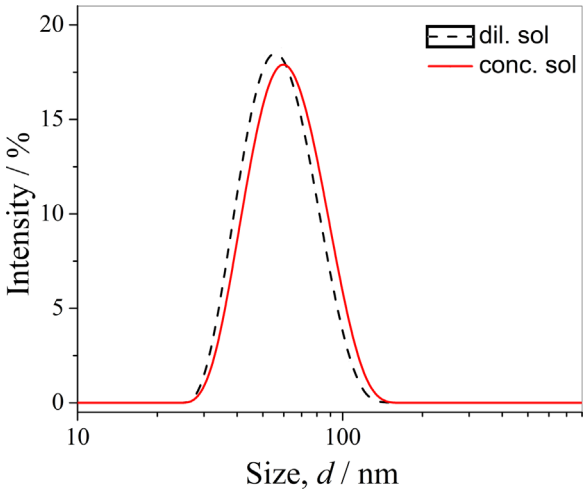

Figure 1. Particle size distribution of ceria sols.

inhibitor when introduced in the corrosive media. In view of the above, the aim of this study was to use a CeO_2 sol to deposit a ceria film onto AA7075 and advance understanding on the corrosion inhibition effect of ceria, i.e. get insight into the mechanism through which cerium oxide particles are able to improve corrosion resistance of the metallic substrate. The surface phenomena occurring in the film were followed by various surface and electrochemical techniques and the role of ceria concentration and size of nanoparticles in system reactivity was assessed. In particular, the great potential of in situ Atomic Force Microscopy (AFM) was exploited: AFM enabled monitoring of the topography in real-time (i.e. evolution of ceria film vs time of exposure in aggressive media) and the information was correlated with electrochemical data acquired by electrochemical impedance spectroscopy (EIS).

Experimental

Sol preparation.—For the preparation of films, two ceria sols (stable aqueous colloidal dispersions) of uniform particle size were used. Sols (pH 3.0) differed only by solid phase content: the diluted one had 0.34 wt%, while that of the concentrated one was 0.78 wt%. The sols were prepared by a forced hydrolysis method using cerium(IV)nitrate as precursor, similar to the synthetic procedure described previously.[37] Briefly, 0.1 M HNO_3 (1200 ml) was heated to the boiling point under reflux, followed by a drop-wise addition of an appropriate amount (90 cm^3) of 1.5 N aqueous solution of $Ce(NO_3)_4$, stabilized with HNO_3, (Alfa Aesar, CAS 13093-17-9). The system was vigorously stirred for 24 h and spontaneously cooled down to the room temperature. The obtained sol was dialyzed against deionized water to eliminate the residual nitrates. The solid content was adjusted by ultrafiltration (Amicon cell, PM series (NMWL = 10000) type membranes, i.e. from originally obtained concentration 0.34% to 0.78%.

The forced hydrolysis method[38,39] is based on promoting the deprotonation of hydrated cations by heating the solution at elevated temperatures (90 °C–100 °C). For a metal M with a valence z, the reaction can be written as[38]:

$$n[M(H_2O)_p]^{z+} \rightarrow M_n(H_2O)_{np-m}(OH)_m]^{(nz-m)+} + mH^+ \quad [9]$$

The soluble hydroxylated complexes produced by the hydrolysis reaction form the precursors for the condensation process which leads to the nucleation of particles. They can be generated at the proper rate to achieve nucleation and growth of uniform particles by adjustment of the temperature and pH. Cerium(IV)ion undergoes strong hydration due to its high charge and rapidly hydrolyzes,[40] thus by the addition of nitric acid, the hydrolysis reaction can be controlled (Eq. 9), enabling the formation of monodispersed ceria particles.

The particle size of the prepared sols was measured by dynamic light scattering method (DLS), Instrument ZetaSizer NS (Malvern, UK). X-ray diffraction (XRD) measurements were performed by a Rigaku SmartLab diffractometer. The data were recorded at 30 mA and 40 kV generator settings, using Cu Kα radiation (λ = 0.154178 nm), in the 2θ range 10°–90°, counting 5° min^{-1} in 0.02° steps. The average crystallite size was estimated using the Debye–Scherrer equation. The specific surface area and pore size distribution of the samples were estimated from nitrogen adsorption–desorption isotherms obtained using a Micrometrics ASAP 2020. The samples were firstly degassed at 150 °C for 10 h under reduced pressure. The specific surface area of samples (Sp) was calculated according to the Brunauer, Emmett and Teller (BET) method from the linear part of the nitrogen adsorption isotherm.[40] The total pore volume (V_{tot}) was estimated at $p/p_0 = 0.998$. The mesopore volume and pore size distribution were determined from the desorption isotherm according to the Barrett, Joyner and Halenda (BJH) method.[41] The volume of micropores was calculated based on α-plot analysis.

Micro-Raman scattering measurements were performed at room temperature using a Jobin-Yvon T64000 triple spectrometer system equipped with a liquid-nitrogen cooled CCD detector. The λ = 514.5 nm line of an Ar^+/Kr^+ mixed laser was used as an excitation source. The incident laser power on the samples was kept low in order to prevent heating effects.

Deposition of CeO_2 film.—The aluminium AA7075-T6, was used as substrate (alloy composition, wt%: 5.51 Zn; 2.29 Mg; 1.45 Cu; 0,13 Mn;0.19 Cr; 0.14 Fe). The substrate panels were pre-treated by polishing with SiC paper (1000, 2000 and 4000 grit) and subsequently polished using 1 μm diamond suspensions. After polishing, the substrates were degreased for 10 min in ethanol ultrasonic bath and rinsed with high purity water. Samples surfaces were then marked to ensure the investigation of the same areas by means of different techniques.

In order to study the inhibition effect provided by ceria, so-prepared aluminum panels were immersed for 24 h in ceria sols of different particle concentrations (diluted or concentrated sol), to obtain the coatings of different thickness. Fresh 50 ml ceria sol was used for deposition of film of ceria nanoparticles, with the panel placed at the bottom of the beaker.

The change of the open circuit potential, E_{oc}, of the aluminum alloy during immersion in diluted and concentrated sols, as well as in water pH 3.0, was followed using digital multimeter ISO-TECH, IDM 73.

Surface characterisation of AA7075 and CeO_2 film.—Topographic and Volta potential maps were obtained using AFM (Veeco Multimode Nanoscope IIIa and NT-MDT Ntegra SPM) and Scanning Kelvin Probe Microscopy (SKP-FM) in order to get information on the anodic and/or cathodic nature of different particles and phases present on the surface. These pictures were simultaneously acquired on marked areas, using a tapping mode (AFM) and an interleave mode (SKP-FM).

Complementary investigations were also performed on the same marked areas, using Karl Zeiss EVO-40 Scaning Electron Microscope (SEM) and Energy Dispersive X-ray Spectroscopy (EDXS), to determine semi-quantitatively the composition of the different phases present on the examined surfaces.

The depth composition profiles were recorded by glow discharge optical emission spectroscopy (GDOES), using a Horiba Jobin Yvon GD HR-profiler, to estimate the amount of Ce present on the sample surfaces. The GDOES instrument was equipped with a standard 4 mm diameter anode, a 0.5 m Pashen Runge polychromator with 28 acquiring channels (purged with N for 24 h before the starting of the tests), RF generator (13.6 MHz) and Quantum XP software. An Ar pressure of 650 Pa and an applied power of 25 W were employed as source conditions for analysis. GDOES analysis was carried out shortly after deposition, meanwhile, coated samples were stored in a desiccator with silica gel.

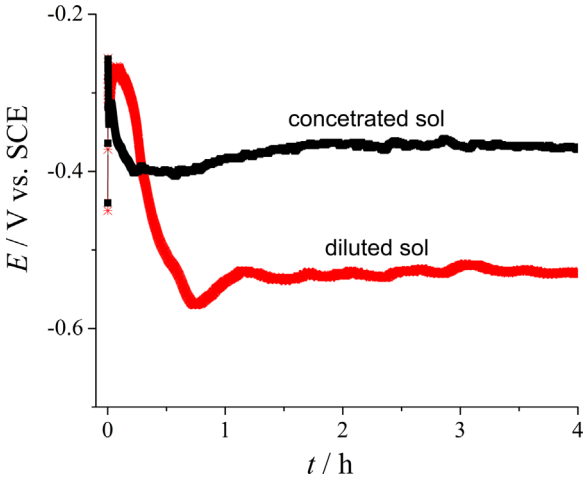

Figure 2. E_{oc} change of AA7075 during immersion in diluted and concentrated CeO_2 sols (pH 3.0).

Corrosion stability was assessed by EIS at E_{oc} in 0.05 mol dm^{-3} NaCl solution, using a Gamry Reference 600 potentiostat/galvanostat/ZRA. The three electrode set up was applied, with bare or coated AA7075 as working electrode (surface 1 cm^2), Pt mesh, of considerably greater surface area, as counter electrode and saturated calomel electrode (SCE) as reference electrode, with 10 mV amplitude, and in frequency range 10 mHz–10^5 Hz. The measurements were performed in an aerated open cell, volume 250 ml, pH 6.5, temperature 23 °C ± 1 °C.

Results and Discussion

The synthesized ceria sols were stable and of the following characteristics: final pH 3.0, highly positively charged particles (Zeta, ζ-potential = 51.2 ± 0.5 mV), sols were monodispersed and composed of evenly sized spherical particles (polydispersity index, PdI = 0.078). Particle size distribution of diluted and concentrated sols given by intensity is shown in Fig. 1. As seen, the hydrodynamic particles size (diameter) of both sols was in the range 30–110 nm, with a Zav (average size) of about 60 nm, confirming that an increase in the solid phase content did not affect the sol stability.

The synthesized ceria was of the fluorite-type crystal structure, as confirmed by XRD (Supplementary material, Fig. S1 is available online at stacks.iop.org/JES/167/101503/mmedia). The broadening of the diffraction peaks (indexed according to the JCPDS 034-394 card) indicated the formation of nano-sized ceria. A very small crystallites size of 3 nm was estimated.

The Raman data corroborated the XRD data, Fig. S2b. The broad asymmetric band that dominates the spectrum is positioned at 456 cm^{-1}. It corresponds to the F2g Raman active mode of the fluorite structure, belonging to the Fm3m space group.[42] A strong asymmetry of the peak as well as its large width indicates a small crystallite size.[43] Besides the main band, the small mode at 605 cm^{-1} is ascribed to the intrinsic oxygen vacancy mode (VO), which originates from the formation of Ce^{3+}–VO complexes in the ceria lattice and is usually very prominent in nanocrystals. This confirms the presence of Ce^{3+} ions in the CeO_2 crystallites, since oxygen vacancies compensate the effective negative charge associated with the trivalent ions.[44]

As determined by adsorption/desorption isotherm of N_2, (Fig. S3a), the ceria nanoparticles exhibit a high specific surface area, S_p = 81 m^2 g^{-1}. The isotherm is reversible at lower equilibrium pressures, with hysteresis loop H2 at higher equilibrium pressures ($p/p_0 > 0.4$) and plateau at high equilibrium pressures ($p/p_0 > 0.9$). Therefore, this isotherm is of type IV, according to the IUPAC nomenclature.[45] The ceria sol is thus dominantly mesoporous material with unimodal narrow pore size distribution (4–8 nm) and a peak at 5.12 nm (Fig. S3b, Table SI).

The CeO_2 deposition on the aluminium alloy was studied by following the change of the E_{oc} during immersion in diluted and concentrated sols, as shown in Fig. 2. Three stages could be observed during CeO_2 deposition on AA7075. The initial sharp E_{oc} increase to ∼–0.27 V, during the first ∼15 s, is related to dissolution of less noble elements relative to matrix, probably Zn from Zn-rich intermetallic particles. It is followed by a distinct E_{oc} decrease to –0.40 or –0.57 V in concentrated and diluted sols, respectively, due to thinning and removal of the natural oxide layer, respectively. Namely, at pH values below 4.0, aluminium oxide is not stable and it dissolves.[46] This surface activation is a well known, necessary first step in the deposition of conversion film on aluminum.[47–49]

The increase in E_{oc}, reaching a potential plateau during extended AA7075 immersion in sols, is the final step in ceria film deposition, resembling nucleation and growth of the ceria film obtained via a pH-driven process.[47–49] The constant E_{oc} value of ∼–0.54 V was reached after over 1 h in diluted sol. Due to the greater amount of cerium hydrated oxide in concentrated sol, the deposition occurs more rapidly, resulting in faster (20 min immersion) increase in E_{oc} in this media (plateau at ∼–0.37 V).

After 24 h immersion of AA7075 in the ceria sols, the obtained films were inspected by GDOES. The composition profiles of the ceria films deposited from diluted and concentrated sols are shown in Fig. 3.

First of all, it has to be stressed that as the surface roughness has the same dimensional range of the thickness of both films, the evaluation of this parameter is approximate. Anyway, to try to obtain

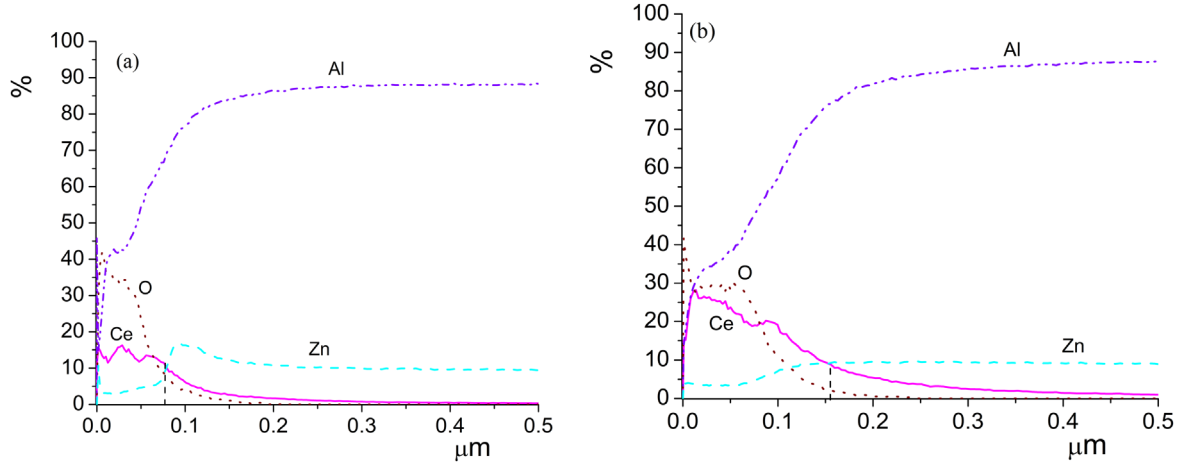

Figure 3. GDOES compositions profiles of AA7075 coated with CeO_2 from: (a) diluted and (b) concentrated sol, dipping time 24 h.

meaningful data these thicknesses were estimated at the intersection of the profiles of the Ce and Zn signals, one element representing only the film and the other one being present only in the substrate. By looking to this intersection it is quite evident that the film deposited from the concentrated sol is thicker (about 160 nm) with respect to the one obtained in the diluted bath (about 70 nm). Also the Ce concentration appears to be higher (about 20%–25%wt) when the film is obtained in the concentrated solution while the diluted ceria sol gives rise to about 15%wt of Ce.

It is likely that the concentration of Ce in the sol is directly correlated to the deposit thickness as well as to the Ce content in the deposit.

Both oxygen profiles correlate well with the Ce trends, suggesting the formation of a cerium oxide film. Nevertheless, curiously the oxygen concentration in the profile relevant to the film obtained in the diluted solution is higher with respect to the other one. As also the aluminum signal is higher in this sample, it is possible to suppose that the thinner layers can be more affected by surface contamination, then suggesting a better coverage and a denser film formation when using the concentrated solution.

Moreover, the Zn profile shows occasionally a slight peak at the deposit/substrate interface. This enrichment could be linked to the presence of intermetallic particles near to the surface due to rolling operations.[50]

The morphological changes in different samples were followed by AFM. The topographic (Fig. 4a) and SEM image (Fig. 4d) of Al surface show a typical morphology of the polished and degreased sample. The measured root mean square, RMS, was 29 nm. The Volta potential difference between intermetallics and alloy matrix was determined by SKPFM,[51–56] on the same area as topographic images in Fig. 4a. Regions with different Volta potentials could be seen from the Volta potential map in Fig. 4b.

The intermetallics can be clearly recognized by an intense contrast in Fig. 4. The Volta potential along the scan line indicated in Fig. 4b is shown in Fig. 4c. The bright spots observed have a Volta Potential about 190 mV higher than Al matrix (Fig. 4c). The existence of a positive Volta potential relative to the aluminum matrix is an indication of the cathodic behavior of the Al-intermetallics. A similar behavior of IMPs was reported in literature, and the cathodic ones claimed as preferential sites for the onset of localized attack due to the galvanic coupling with aluminum matrix.[57,58] Namely, the Volta potential difference between intermetallics and matrix provides the electrochemical driving force for the onset of Al dissolution.[59,60]

SEM micrographs of the polished AA7075 surface at different magnifications are reported in Figs. 4d and 4e. According to the EDX analysis, sites 1 and 2 of Fig. 4d correspond to large Fe rich intermetallics (13.34 and 11.10 wt%% Fe, respectively), containing also smaller amounts of Cu and Zn (2.86 wt% Cu, 3.61 wt% Zn and 3.49 wt% Cu, 4.77 wt% Zn, respectively). The site 3 corresponds to an intermetallic containing 4.10 wt% Mg, 1.94 wt% Cu, 7.27 wt% Zn. The white small particles marked as 4 and 5 in Fig. 4e correspond to the Zn-rich IMPs (11.96 and 12.16 wt% Zn and 4.02 and 3.86 wt% Mg respectively).

Morphological and potential changes after 24 h immersion in diluted CeO_2 sol are shown at the same area as for bare AA7075, Fig. 5. The polishing features are no longer visible, denoting the film formation on the surface. In addition, the presence of numerous bright spots could be noticed, related to cerium oxide particles (Figs. 5a, 5b 5d). The SEM and EDXS analyses confirmed the presence of low amounts of Ce (up to 0.75 wt%); Fe-rich IMP on the Al matrix is marked by 1 in Fig. 5d and two other intermetallics, marked as 2 and 3, contain Mg and Zn (5.52 and 7.98 wt% Zn and 1.27 and 2.44 wt% Mg respectively). Considering the small thickness of the ceria film these results could not be taken as reliable for the Ce quantification.

The topography indicated an increased roughness (56 nm vs 29 nm for Al), due to the ceria film deposited on the surface (Fig. 5a). The film is composed of ceria nanoparticles, organized in the form of bigger or smaller aggregates, appearing as sharp islands, which almost continuously cover the surface. Unlike CeCCs obtained from Ce–salts,[61,62] exhibiting cracked/dry mud morphology, this ceria film did not clearly show cracks (Fig. 5b).

As observed (Fig. 5c), the Volta potential difference was reduced and almost no potential differences could be seen in the analyzed area. The section analysis, carried out along the line as in Fig. 5a with pronounced differences in topography, indicated small Volta potential differences of ~7 mV. The lowering of potential differences on bare AA7075 results from the CeO_2 film uniformly deposited over the alloy surface.

The morphology of ceria film obtained from concentrated sol, along with Volta potential map, is presented in Fig. 6. It is also composed of differently sized aggregates, randomly distributed on the surface. It is obvious that this covering film is more compact and much rougher, RMS 114 nm, in comparison with thinner film, derived from diluted sol. A great number of aggregates seem to be sticking out, due to the pronounced height and sharp tips. Regardless of differences in roughness along the surface, the Volta potential (Fig. 6c) remained below 5 mV, similar to the value measured for thin film obtained from diluted sol.

Since the Volta potential difference was strongly reduced (from around 200 mV) after immersion in the CeO_2 sols, it can be considered that the deposition of Ce-species took place both on intermetallics and on aluminum matrix. In other words, the deposition of ceria led to the de-activation of the cathodic sites, reducing the Volta potential difference between IMPs and Al matrix.

In order to determine the effect of deposited CeO_2 films on the corrosion stability of aluminium alloy, EIS measurements were recorded for bare and ceria-coated AA7075 in 0.05 mol dm^{-3} NaCl solution at different immersion times (Figs. 7 and 8). The Bode plots in Fig. 7 display the evolution of impedance for bare aluminium surface, as well as for ceria film obtained from diluted sol during immersion in NaCl solution. After the first hour of immersion (Fig. 7a), the total impedance of AA7075 at the lowest $|Z|$ was ~3000 Ω cm^2 and it did not change much during the following few hours. This initial time of exposure was characterized with one-time constant in the middle frequency range (Fig. 7b). After about 6–7 h another time constant developed in the phase angle spectrum in the frequency range 10–100 mHz. This was accompanied by the increase of the total impedance modulus at the lowest $|Z|$ and after 24 h immersion it was (~5000 Ω cm^2).

There are some interesting features in EIS spectra recorded for thin CeO_2 film (derived from diluted sol) on the Al alloy, Fig. 7. Namely, the CeO_2 film increased the impedance at low frequency to ~$1.6 \cdot 10^4$ Ω cm^2 after the first hour of immersion and after 2 h, the impedance value further increased (Fig. 7a). However, given the very small thickness of CeO_2 film (70 nm), this thin film could provide only a short-term protection, displayed by the impedance drop upon further exposure. Finally, after 24 h the ceria impedance reached the value of bare AA7075. Two well pronounced time constants were present and there was a slight shift of the phase angle towards higher values in the middle frequency range after 2 h immersion, decreasing towards the aluminium values during longer immersion.

Corrosion behaviour of the thicker ceria film, deposited from concentrated sol, was also followed during exposure to NaCl. The improved corrosion stability imparted by this film is clearly visible in Fig. 8.

The initial total impedance modulus at the lowest frequency was ~8000 Ω cm^2 and it gradually increased during immersion time, to reach ~$2.2 \cdot 10^4$ Ω cm^2 after 7 h (Fig. 8a). Two well established time constants could also be seen in Fig. 8b. The broadening of the phase angle peak at middle frequencies with immersion time could be observed, accompanied with the shift of phase angle peak to higher degrees. After nine hours of exposure to NaCl solution the total impedance values started decreasing and after 24 h (Fig. 8a) reached the values of AA7075 (Fig. 7a). The beneficial effect of this ceria film on Al protection was more pronounced as compared to the one derived from diluted sol, which provided only a short term protection.

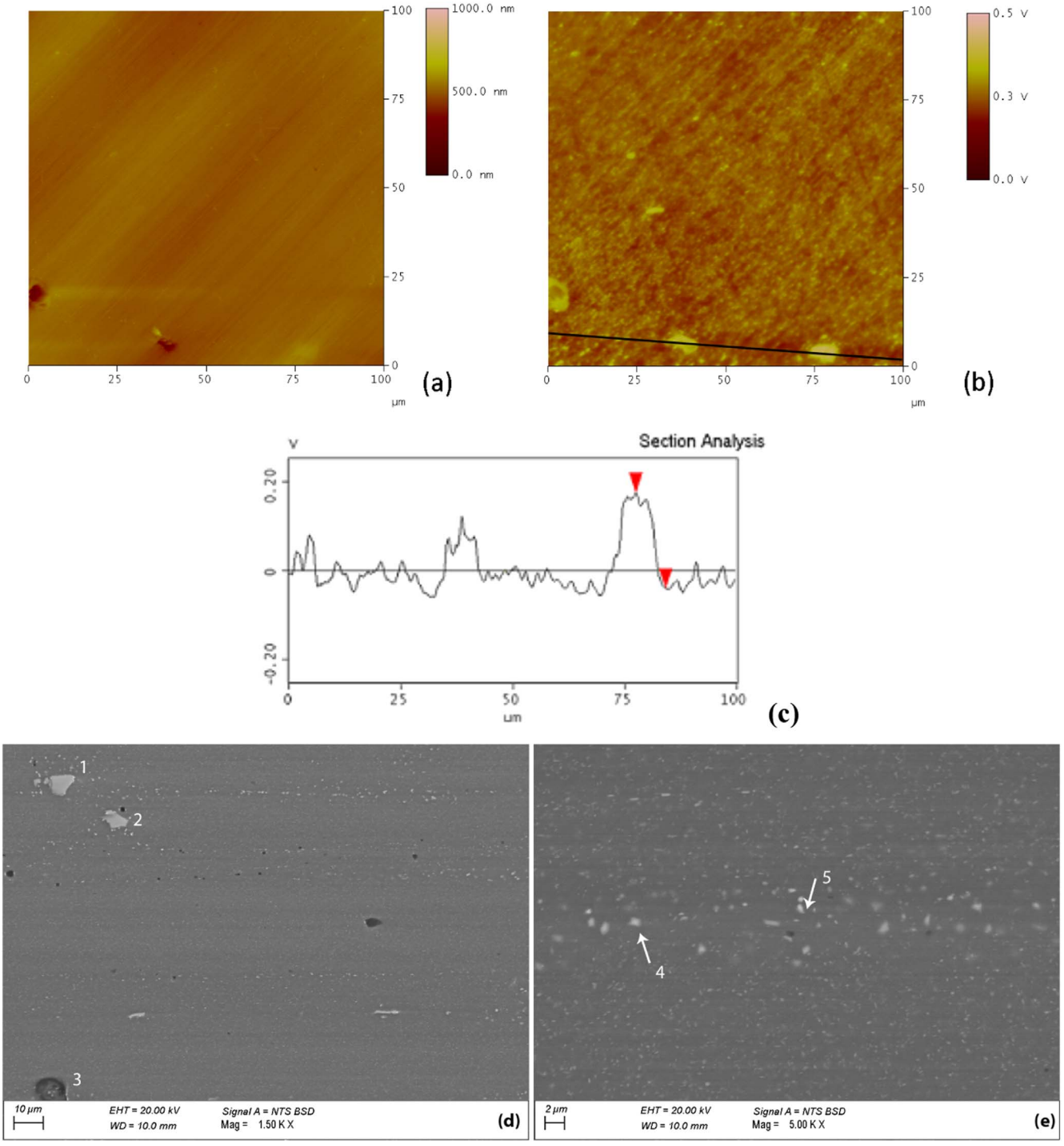

Figure 4. (a) AFM topographic map, (b) SKPFM Volta Potential map and (c) section analysis, (d) and (e) SEM image of polished and degreased AA7075 substrate at different magnifications.

The differences among the samples could be better seen in Fig. 9, after 7 h of exposure to NaCl solution. Namely, the CeO_2 film obtained by deposition from concentrated sol increased the low-frequency impedance 5 times ($\sim 2.2 \cdot 10^4$ Ω cm^2) compared to that registered for the ceria film deposited from diluted sol ($\sim 6.0 \cdot 10^3$ Ω cm^2) and bare AA7075 ($\sim 4.2 \cdot 10^3$ Ω cm^2). The time constant in the middle frequency range is related to responses of both ceria film and aluminium oxide and there was a pronounced phase angle shift for the thicker ceria film, although not exhibiting capacitive behavior. All these suggest the active protection provided by ceria film deposited from concentrated sol, or possibly the development of corrosion products on the surface.

As it was intriguing to distinguish between the two and detect the changes taking place on the surface during exposure to a corrosive solution at open circuit potential, an in situ AFM monitoring of bare and ceria coated AA7075 was applied for varying times and results are presented in Figs. 10–12.

The AA7075 sample upon exposure to NaCl solution is shown in Fig. 10. After 1 h of immersion, the bright spots were easily visible and their number increased significantly after 3 h, probably marking the spots of the corrosion onset.

In situ AFM characterization of the ceria film deposited from diluted sol, during exposure to NaCl solution was followed for three hours, at open circuit potential. The 2D and 3D images, taken after

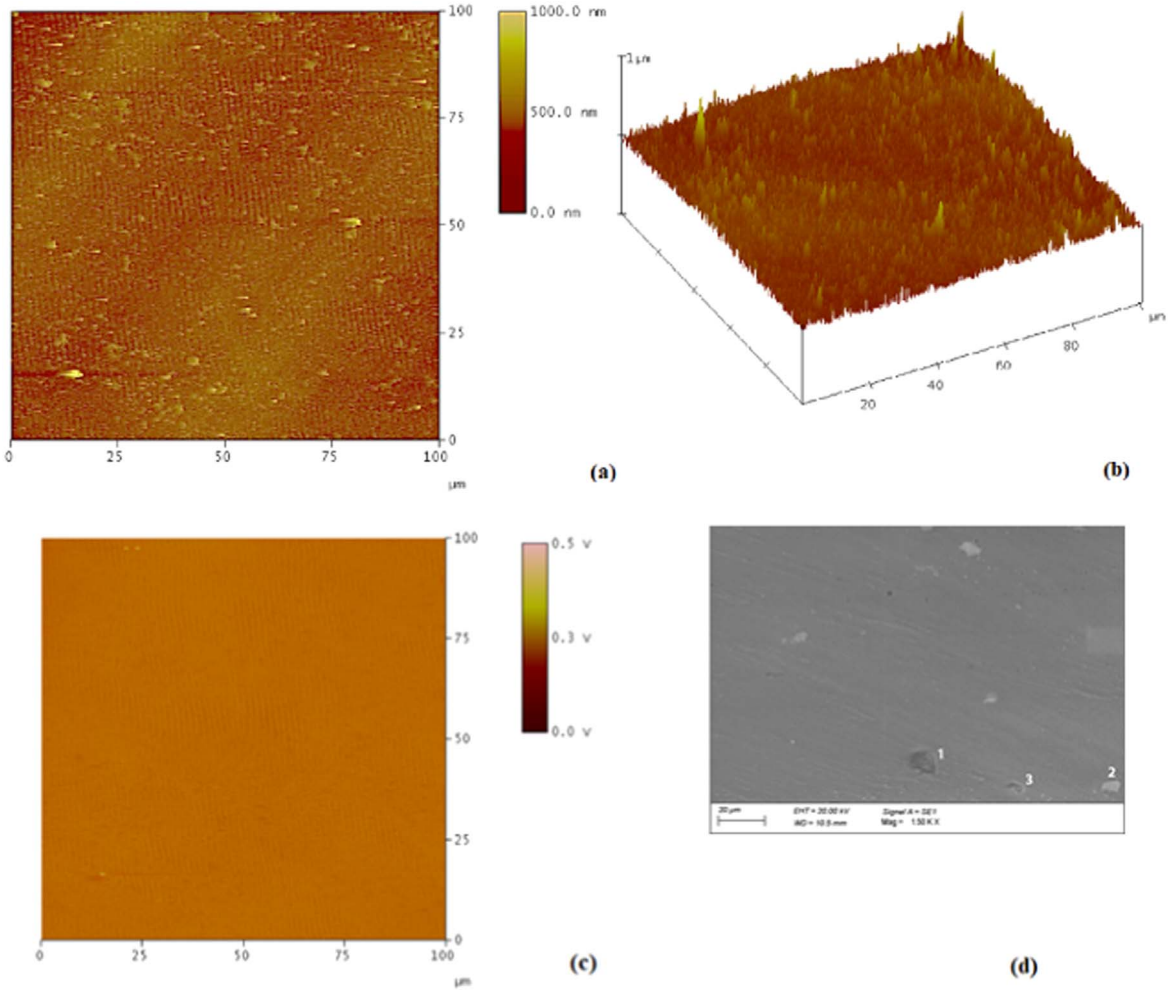

Figure 5. (a) 2D and (b) 3D AFM topographic map, (c) SKPFM Volta Potential map of CeO_2 film deposited from diluted sol on Al alloy substrate and (d) SEM image of ceria film obtained from diluted sol on AA7075.

30 min immersion (Fig. 11), reveal smaller and bigger aggregates of ceria particles distributed as islands on the substrate. Interestingly, the shape of aggregates changed from sharp to round under effect of NaCl.

Several ceria islands were monitored during this time, and the change in their number and size is shown in Fig. 12. A surface area displaying two large deposits, surrounded by smaller ones was selected. Considering the size of ceria particles in diluted sol (hydrodynamic diameter ~60 nm) the bright spots in Fig. 12a actually represent CeO_2 aggregates. Their dimensions were noticed to fluctuate with time of exposure to the aggressive media. After 20 min, the aggregates became smaller in size (Fig. 12b), followed by their further increase (Fig. 12c) and decrease (Figs. 12d and 12e). The size of a small island placed between two big ones, also changed, i.e. decreased, and after 3 h immersion it was hardly recognizable by AFM.

The evolution in size of these CeO_2 aggregates was measured in parallel by section analysis. It was confirmed that the originally determined sizes of 1.07 and 0.705 μm (indicated by cursors in Fig. 12a) reduced to 0.877 and 0.614 μm after 20 min (Fig. 12b), further increased to 1.14 and 0.909 μm after 100 min (Fig. 12c) and changed to 1.05 and 0.939 μm after 2 h (Fig. 12d). After 3 h, there was a marked drop in aggregate sizes, to 0.850 and 0.695 μm (Fig. 12e).

Besides the change in width, the height of aggregates was also oscillating. Namely, after the first few minutes in NaCl solution, the surface distance (length of line between cursors in section analysis) dropped from initial 1.09 and 0.779 μm to 0.906 and 0.721 μm after 20 min, further increased to 1.23 and 0.942 μm after 100 min and after 2 h to 1.11 and 1.00 μm. Finally, they were of 0.890 and 0.711 μm after 3 h. In other words, a re-arrangement in the ceria film occurred: particles desorbed/detached and re-deposited/re-adsorbed during exposure to NaCl, but the effect became less pronounced after 3 h. In parallel, the height/thickness of film, composed of smaller aggregates, between the followed big ones, continually decreased. Although the local re-deposition/re-adsorption around already existing bigger aggregates seems to be a dominant process, small CeO_2 aggregates/particles disappeared over immersion time, (Fig. 12). As seen in Fig. 12e, the surface between the followed 2 big aggregates became impoverished with ceria particles, giving a mixed EIS response and resulting in reduced protection (Fig. 7).

This was a quite unusual finding**,** since ceria is known for small solubility constant.[63] However, according to the Ostwald-Freundlich equation,[64] ceria particles of the nanometric size easily dissolve. The dissolution rate of CeO_2 was also reported to increase with increasing surface area.[65] The greater the portion of intrinsic defects and oxygen vacancies the higher the dissolution rate. Grain boundaries thus preferentially dissolve due to increased number of energetically reactive sites compared to the surfaces. Greater solubility of Ce^{3+} vs Ce^{4+} accelerates the dissolution kinetics.[63,65] It is known that the fraction of Ce^{3+} is very prominent in nanocrystals and that the ions are situated at the grain boundaries. This, in turn, facilitates preferential dissolution along the boundaries, resulting in diminution of particle size.[66]

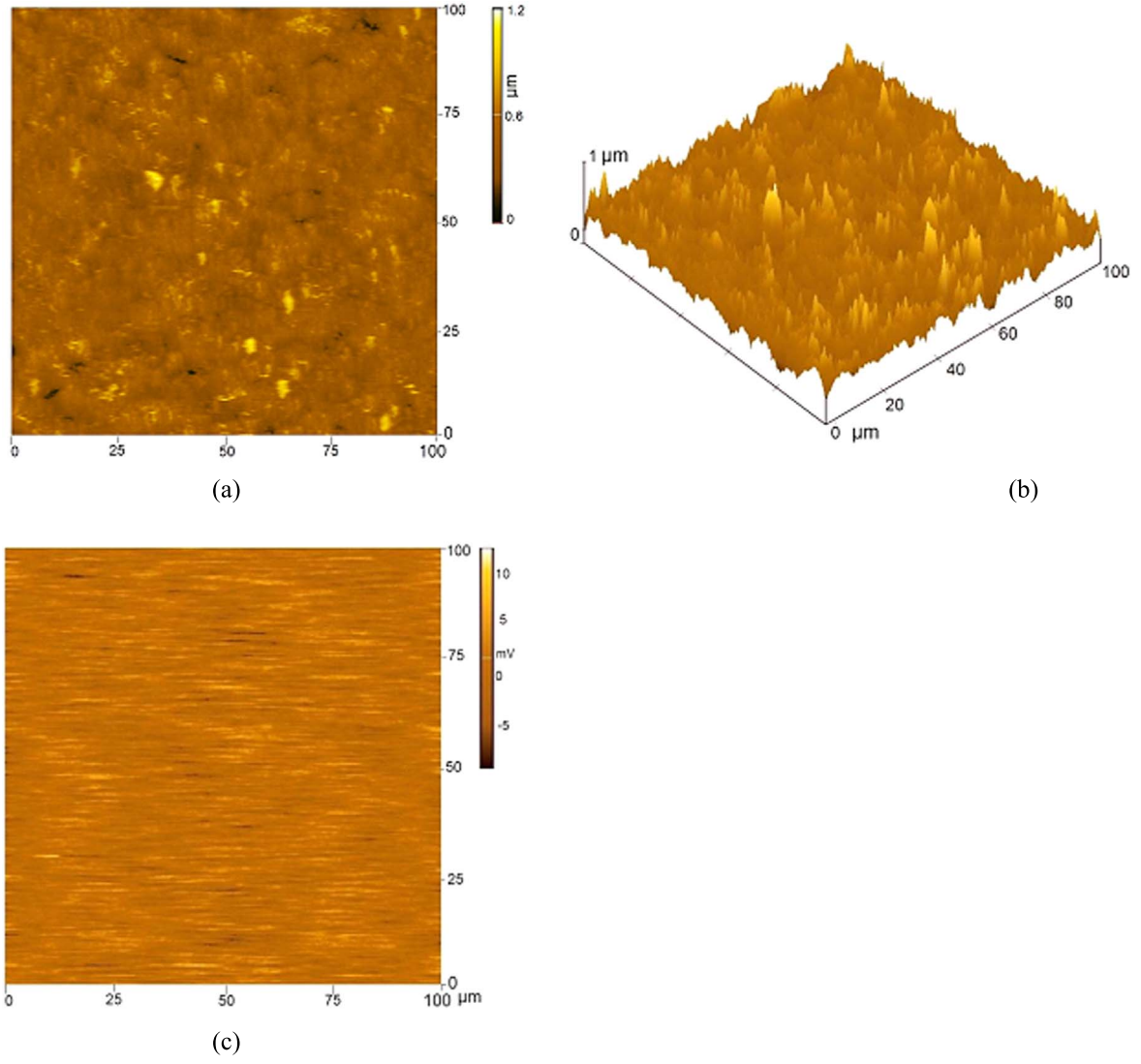

Figure 6. (a) 2D (100 μm × 100 μm) and (b) 3D AFM topographic map (100 μm × 100 μm × 1 μm) and (c) SKPFM Volta Potential map of CeO_2 film deposited from concentrated sol on AA7075 substrate.

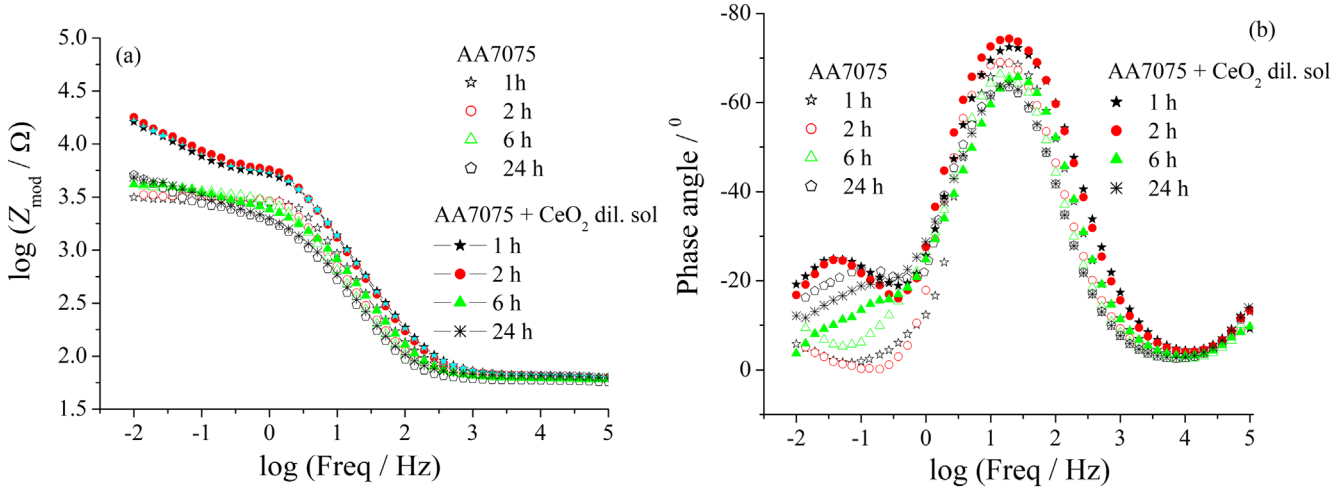

Figure 7. Bode: (a) modulus and (b) phase angle plots for AA7075 and CeO_2 film deposited from diluted sol on AA7075 substrate during immersion in 0.05 mol dm^{-3} NaCl.

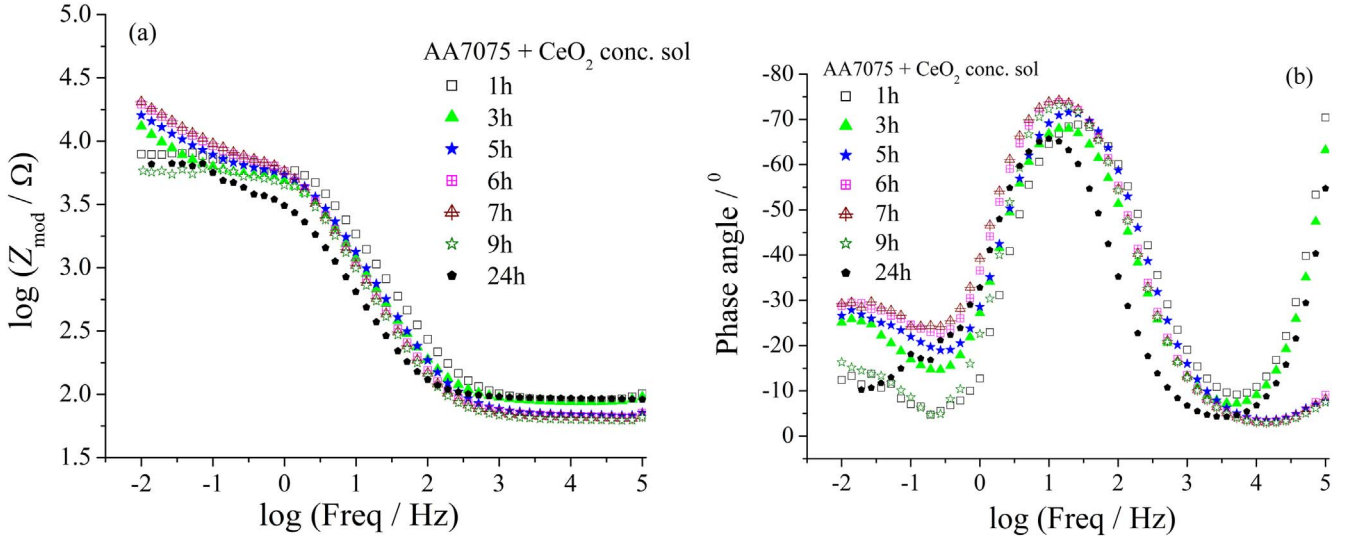

Figure 8. Bode: (a) modulus and (b) phase angle plots for CeO_2 film deposited from concentrated sol on AA7075 substrate during immersion in 0.05 mol dm^{-3} NaCl.

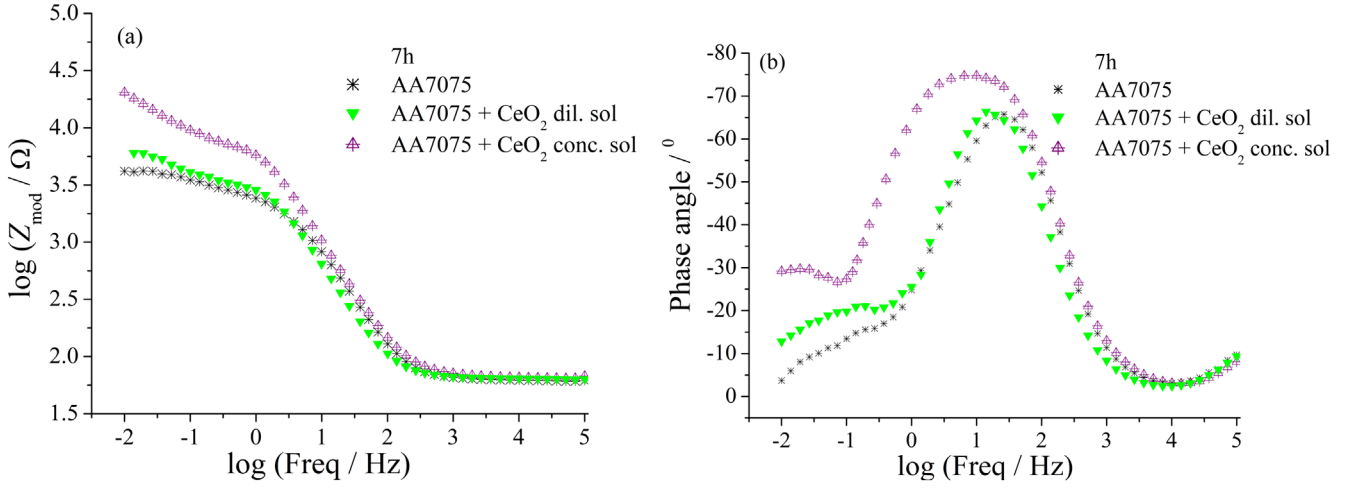

Figure 9. Bode: (a) modulus and (b) phase angle plots for CeO_2 film deposited from diluted and concentrated sols and AA7075 after 7 h immersion in 0.05 mol dm^{-3} NaCl.

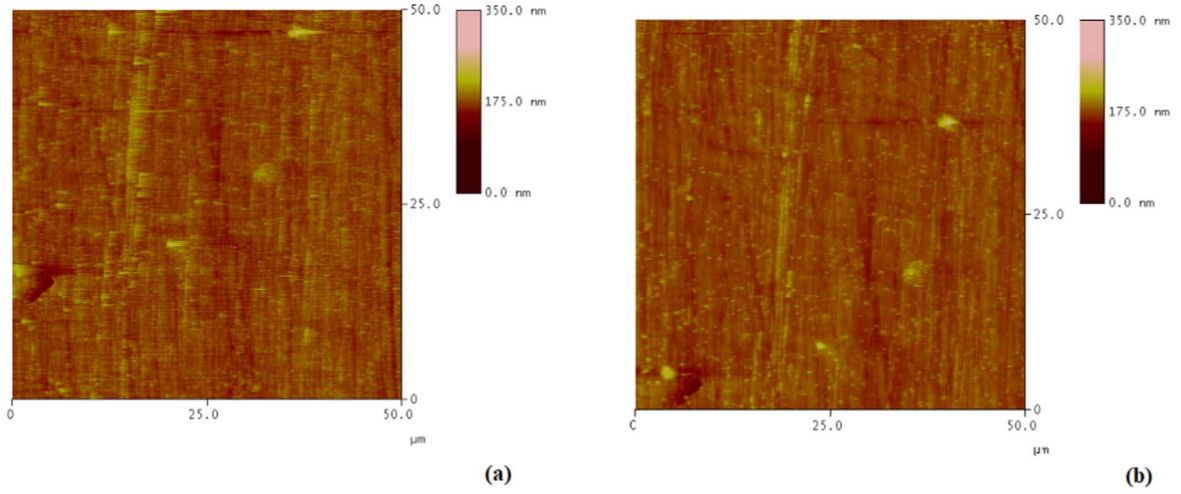

Figure 10. In situ AFM monitoring of bare AA7075 after: (a) 1 and (b) 3 h in 0.05 mol dm^{-3} NaCl.

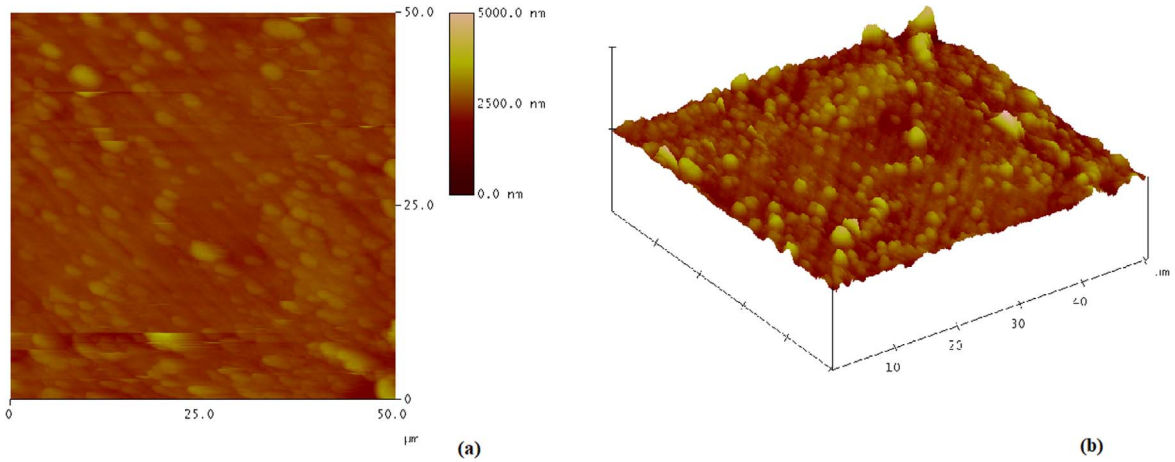

Figure 11. In situ AFM monitoring (a) 2D and (b) 3D of CeO_2 deposit obtained from diluted sol after 30 min in 0.05 mol dm^{-3} NaCl.

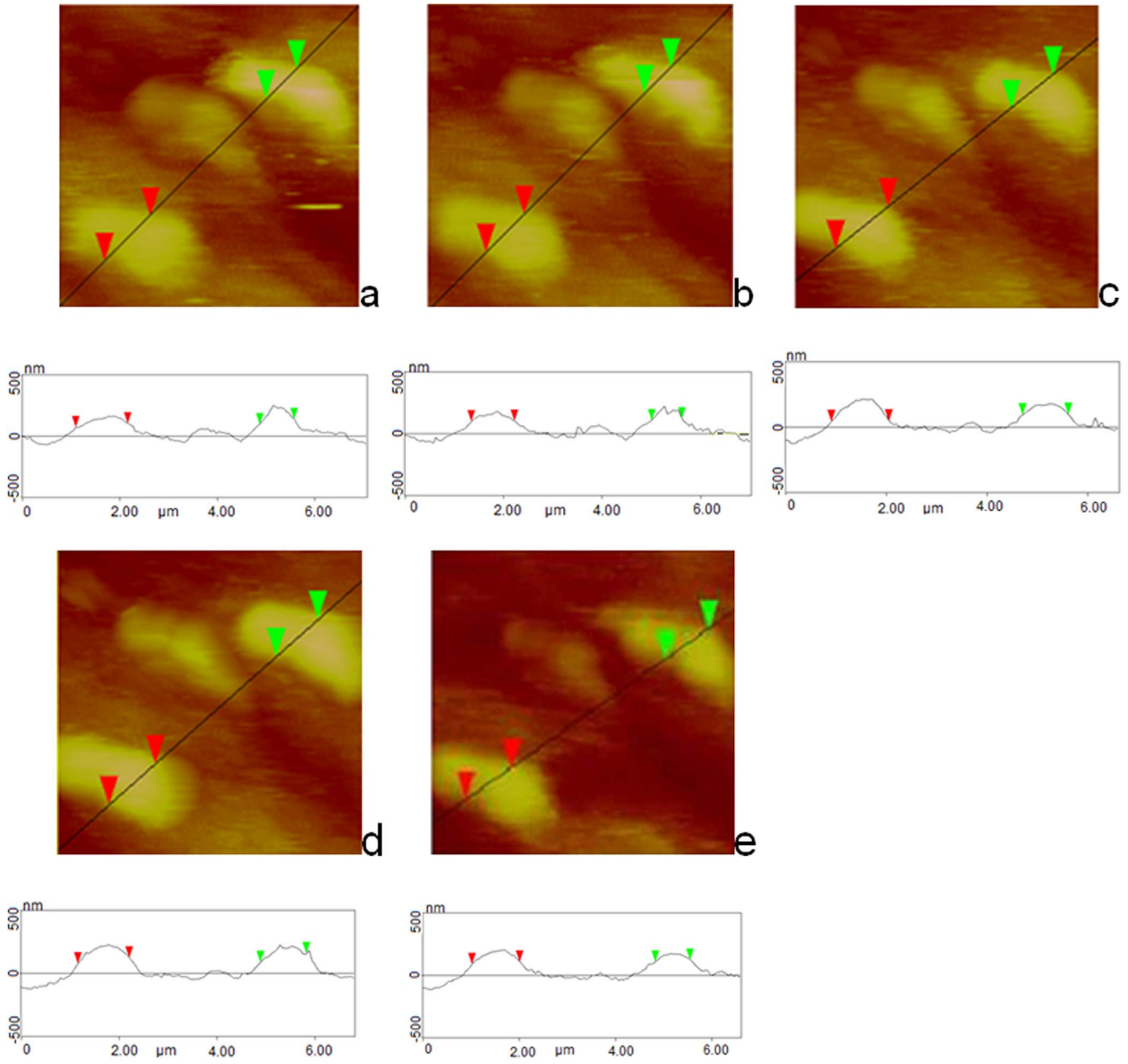

Figure 12. In situ AFM monitoring (5 × 5 × 1 μm) of CeO_2 films obtained from diluted sol and corresponding section analysis after: (a) few minutes, (b) 20 min, (c) 100 min, (d) 2 h and (e) 3 h, in 0.05 mol dm^{-3} NaCl.

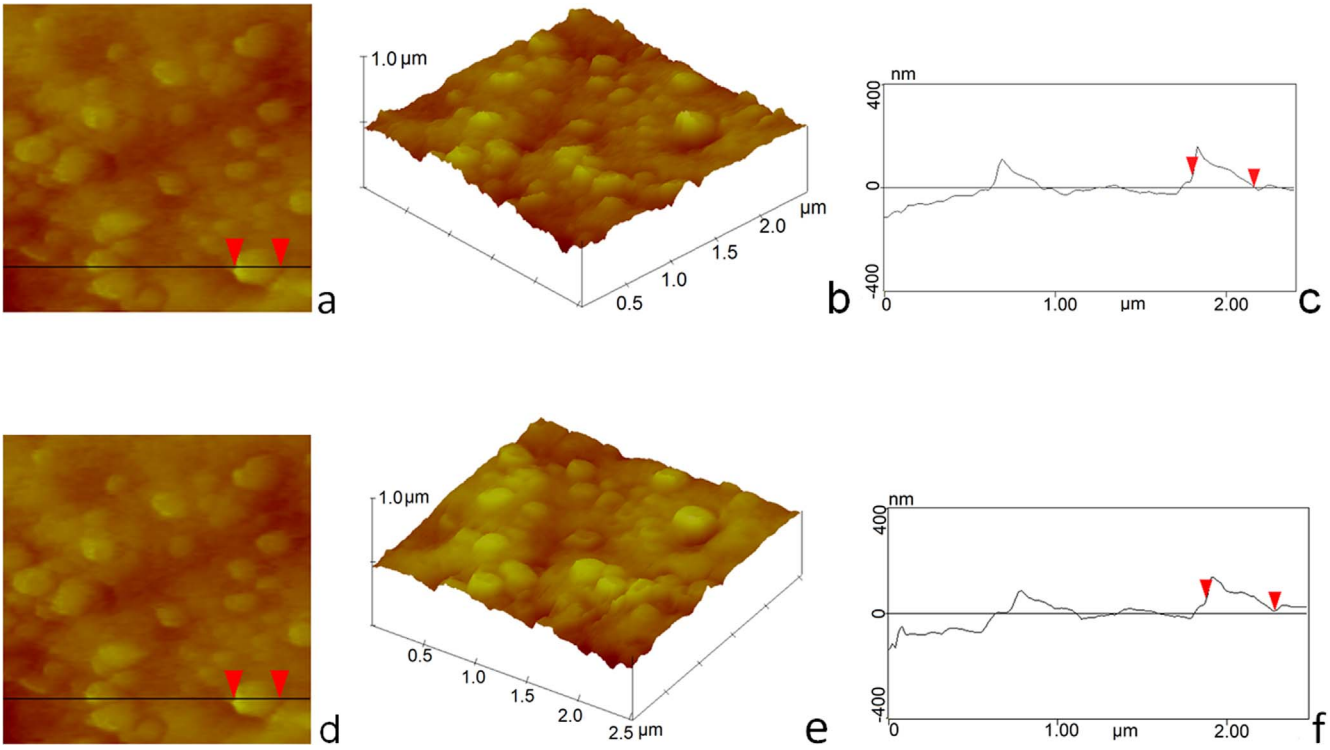

Figure 13. In situ AFM monitoring of CeO_2 films obtained from concentrated sol: 2D (a) and (d), 3 D (b) and (e) and corresponding section analysis (c) and (f) after: 2 h (a)–(c) and 3 h (d)–(f) in 0.05 mol dm^{-3} NaCl.

Since the employed ceria sol was nano-sized, possessing considerable *Sp* value, mesoporosity and fraction of Ce^{3+} ions, from a macroscopic approach, it can be hypothesized that an analogous process occurred in the ceria film during immersion in aggressive NaCl solution, being composed of aggregated nanoparticles deposited on AA7075. Namely, rather fast disintegration of ceria aggregates (i.e. desorption/detachment/dissolution of particles) took place, producing individual sized smaller particles, which were capable of further re-deposition/re-arrangement in the film.

The evolution in surface morphology of thicker ceria film during exposure to NaCl solution was also followed by in situ AFM, Fig. 13. The similar feature of the change in shape of aggregates upon immersion in NaCl solution was observed. The aggregates of extreme heights were no longer visible. Instead, rounded aggregates of similar size covered the Al surface. We assume that the leveling of this ceria film occurred due to the presence of small aggregates-constituents of the ceria film deposited on the surface. Thus, the process of detachment/re-deposition of particles was facilitated and more rapid, resulting in more homogeneous ceria film. We believe that sharp tips present in thicker film disintegrated upon exposure to NaCl solution. The released particles further rearranged, forming a more compact structure with reduced roughness. Indeed, a cross sectional analysis indicate that the aggregate size of 361 nm, determined after 2 h exposure was enlarged to 407 nm after 3 h of exposure.

It is likely that the enlargement/reduction of size of the ceria aggregates during exposure to NaCl solution, shown by in situ monitoring (Figs. 12 and 13), originate from the dynamic process of ceria particles dissolution/detachment/re-deposition. The effect is more pronounced in the film deposited from the concentrated sol, owing to the greater amount of Ce available in the thicker film. In addition, a rather uniform and compact film structure that developed upon immersion in NaCl solution was also beneficial for maintaining higher impedance values during longer time.

The scheme of the whole process is presented in Fig. 14, starting from the bare AA7075, with considerable Volta potential differences originating from the presence of IMPs (Fig. 14a). This potential difference was reduced upon ceria film deposition (Fig. 14b). The dynamic process of desorption and redeposition of particles occuring

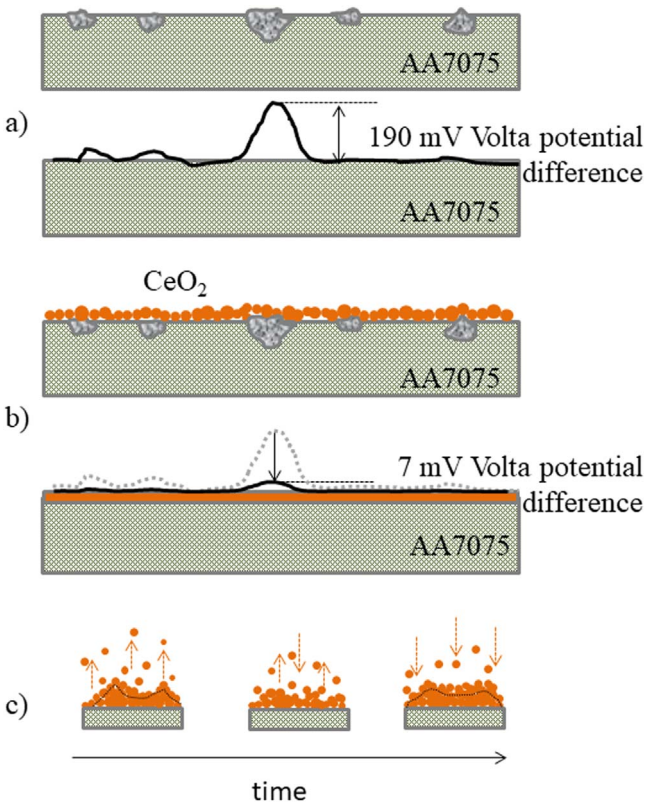

Figure 14. Schematic presentation: (a) bare AA7075, (b) CeO_2 film on AA7075 and (c) evolution in ceria film morphology upon immersion in NaCl solution.

in the ceria film during immersion in NaCl solution is schematically presented in Fig. 14c. The sharp tips of aggregates of different sizes in ceria film disintegrated, the released particles further re-deposited/re-arranged in the film, forming a more compact structure of reduced roughness.

Conclusions

Ceria films were successfully deposited by 24 h immersion in diluted and concentrated aqueous ceria sols (pH 3.0) on the surface of AA7075. Thinner (70 nm) and thicker (160 nm) films were obtained respectively, as detected by GDOES. OCP real-time monitoring suggested that the deposition of ceria is a 3-step process: dissolution of the native oxide film, followed by ceria film formation. SKPFM indicated that the Volta potential differences between intermetallic alloying particles and surrounding aluminium matrix of around 190 mV were reduced significantly (to 5–7 mV) upon ceria film deposition onto the metallic surface.

EIS response collected in 0.05 mol dm^{-3} NaCl confirmed that even a thin ceria film on the AA7075 surface increased by five times the initial low frequency impedance, although providing only a short term protection (up to 3 h). A thicker film imparted longer protection (immersion time 2–7 h) and it remained significant even after 24 h.

A correlation between evolution of ceria film topography and impedance response was presented. As deposited films exhibited simmilar morphological features: both were composed of differently sized ceria aggregates forming a rough surface, due to the presence of numerous sharp aggregates. In situ AFM provided monitoring of change in size (width and height) of the ceria aggregates, constituents of the ceria film, during exposure to the aggressive media.

Results indicated that the change in corrosion behaviour resulted from the morphological change/phenomenon occuring on the AA7075 surface. The most pronounced change upon exposure to NaCl was a dissapearance of the sharp tips and formation of round surfaces of the aggregates instead. We believe that the ceria film started to disintegrate during exposure to NaCl, but also to re-assemble and recover. Small ceria particles seemed to dissolve/detach rather fast, while, in parallel, larger particles grew at their expense. The rearangement led to more compact protective film with reduced roughness-leveling of the film. This dynamic process, resulting from the ceria nanometric particle size and reactivity, was the origin of the variable EIS response.

Acknowledgments

This research was funded by the Ministry of Education, Science and Technological Development of the Republic of Serbia (Contract Nos. 451-03-68/2020-14/200135 and 451-03-68/2020-14/200017). The authors would like to acknowledge networking support by the COST Action MP1407. Authors also thank Dr. I. Častvan-Janković, Faculty of Technology and Metallurgy, University of Belgrade, for B.E.T. measurements and Dr. Z. Dohčević-Mitrović, Institute of Physics, University of Belgrade, for performing Raman measurement. The authors would like to acknowledge networking support by the COST Action MP1407.

ORCID

Jelena B. Bajat https://orcid.org/0000-0003-0742-8176

References

1. J. Cerezo, P. Taheri, I. Vandendael, R. Posner, K. Lill, J. H. W. de Wit, J. M. C. Mol, and H. Terryn, "Influence of surface hydroxyls on the formation of Zr-based conversion coatings on AA6014 aluminum alloy." *Surf. Coat. Tech.*, **254**, 277 (2014).
2. R. V. Lakshmi, S. T. Aruna, C. Anandan, P. Bera, and S. Sampath, "EIS and XPS studies on the self-healing properties of Ce-modified silica-alumina hybrid coatings: evidence for Ce(III) migration." *Surf. Coat. Tech.*, **309**, 363 (2017).
3. S. S. Golru, M. M. Attar, and B. Ramezanzadeh, "Morphological analysis and corrosion performance of zirconium based conversion coating on the aluminum alloy 1050." *J. Ind. Eng. Chem.*, **24**, 233 (2015).
4. B. Valdez, S. Kiyota, M. Stoytcheva, R. Zlatev, and J. M. Bastidas, "Cerium-based conversion coatings to improve the corrosion resistance of aluminium alloy 6061-T6." *Corr. Sci.*, **87**, 141 (2014).
5. R. S. Gharabagh and A. S. Rouhaghdam, "Corrosion of environmentally friendly lanthanum conversion coating on AA2024-T3 aluminum alloy." *Prot. Met. Phys. Chem. Surf.*, **50**, 88 (2014).
6. B. V. Jegdić, L. S. Živković, J. P. Popić, J. B. Bajat, and V. B. Mišković-Stanković, "Electrochemical methods for corrosion testing of Ce-based coatings prepared on AA6060 alloy by the dip immersion method." *J. Serb. Chem. Soc.*, **78**, 997 (2013).
7. Q. S. Yao, F. Zhang, L. Song, R. C. Zeng, L. Y. Cui, S. Q. Li, Z. L. Wang, and E. H. Han, "Corrosion resistance of a ceria/polymethyltrimethoxysilane modified Mg-Al-layered double hydroxide on AZ31 magnesium alloy." *J. Alloys Compd.*, **764**, 913 (2018).
8. L. G. Ecco, M. Fedel, F. Deflorian, J. Becker, B. B. Iversen, and A. Mamakhel, "Waterborne acrylic paint system based on nanoceria for corrosion protection of steel." *Prog. Org. Coat.*, **96**, 19 (2016).
9. M. Eslami, M. Fedel, G. Speranza, F. Deflorian, and C. Zanella, "Deposition and characterization of cerium-based conversion coating on HPDC low Si content aluminum alloy." *J. Electrochem. Soc.*, **164**, C581 (2017).
10. B. V. Jegdic, L. S. Zivkovic, J. P. Popic, J. Rogan, J. B. Bajat, and V. B. Miskovic-Stankovic, "Corrosion stability of cerium-doped cataphoretic epoxy coatings on AA6060 alloy." *Mater. Corros.*, **67**, 1173 (2016).
11. T. T. Thai, A. T. Trinh, and M.-G. Olivier, "Hybrid sol–gel coatings doped with cerium nanocontainers for active corrosion protection of AA2024." *Prog.Org. Coat.*, **138**, 105428 (2020).
12. M. F. Montemor, R. Pinto, and M. G. S. Ferreira, "Chemical composition and corrosion protection of silane films modified with CeO_2 nanoparticles." *Electrochim. Acta*, **54**, 5179 (2009).
13. B. R. W. Hinton, D. R. Arnott, and N. E. Ryan, "Inhibition of aluminum alloy corrosion by cerous cation." *Met. Forum*, **7**, 211 (1984).
14. D. R. Arnott, N. E. Ryan, B. R. W. Hinton, B. A. Sexon, and A. E. Hughes, "Auger and XPS studies of cerium corrosion inhibition on 7075 aluminum alloy." *Appl. Surf. Sci.*, **22/23**, 236 (1985).
15. B. R. W. Hinton, D. R. Arnott, and N. E. Ryan, "Cerium conversion coatings for the corrosion protection of aluminium." *Mater. Forum*, **9**, 162 (1986).
16. A. Uhart, J. B. Ledeuila, D. Gonbeau, J. C. Dupin, J. P. Bonino, F. Ansart, and J. Esteban, "An Auger and XPS survey of cerium active corrosion protection forAA2024-T3 aluminum alloy." *Appl. Surf. Sci.*, **390**, 751 (2016).
17. K. Nakayama, T. Hiraga, C. Zhu, E. Tsuji, Y. Aoki, and H. Habazaki, "Facile preparation of self-healing superhydrophobic CeO_2 surface by electrochemical processes." *Appl. Surf. Sci.*, **423**, 968 (2017).
18. A. De Nicolò, L. Paussa, A. Gobessi, A. Lanzutti, C. Cepek, F. Andreatta, and L. Fedrizzi, "Cerium conversion coating and sol–gel multilayer system for corrosion protection of AA6060." *Surf. Coat. Tech.*, **287**, 33 (2016).
19. M. Santamaria, L. Asaro, P. Bocchetta, B. Megna, and F. Di Quarto, "Anodic electro deposition of CeO_2 and Co-Doped CeO_2 thin films electrochemical/electroless deposition." *J. Electrochem. Soc.*, **160**, D212 (2013).
20. Y. Yang, Y. Yang, T. Fu, J. Zhu, J. Fan, Z. Zhang, and J. Zhang, "Influence of ethanol content in the precursor solution on anodic electrodeposited CeO_2 thin films." *Thin Solid Films*, **556**, 128 (2014).
21. F. Faisala, A. Toghana, I. Khalakhan, M. Vorokhta, V. Matolin, and J. Libuda, "Characterization of thin CeO_2 films electrochemically deposited on HOPG." *Appl. Surf. Sci.*, **350**, 142 (2015).
22. L. S. Živković, B. V. Jegdić, J. P. Popić, J. B. Bajat, and V. B. Mišković-Stanković, "The influence of Ce-based coatings as pretreatments on corrosion stability of top powder polyester coating on AA6060." *Prog.Org.Coat.*, **76**, 1387 (2013).
23. F. Andreatta, M.-E. Druart, A. Lanzutti, M. Lekka, D. Cossement, M.-G. Olivier, and L. Fedrizzi, "Localized corrosion inhibition by cerium species on clad AA2024 aluminium alloy investigated by means of electrochemical micro-cell." *Corr. Sci.*, **65**, 376 (2012).
24. D. K. Heller, W. G. Fahrenholtz, and M. J. O'Keefe, "Chemical and structural analyses of subsurface crevices formed during spontaneous deposition of cerium-based conversion coatings." *Mater. Charact.*, **62**, 1071 (2011).
25. S. Ershov, M. E. Druart, M. Poelman, D. Cossement, R. Snyders, and M.-G. Olivier, "Deposition of cerium oxide thin films by reactive magnetron sputtering for the development of corrosion protective coatings." *Corr. Sci.*, **75**, 158 (2013).
26. Y. Liu, J. Huang, J. B. Claypool, C. E. Castano, and M. J. O'Keefe, "Structure and corrosion behavior of sputter deposited cerium oxide based coatings with various thickness on Al 2024-T3 alloy substrates." *Appl. Surf. Sci.*, **355**, 805 (2015).
27. M. Suda, M. Ogawa, K. Otsuka, K. Nakamura, T. Izu, T. Morita, S. Suzuki, K. Ishibashi, M. Nakamura, and Y. Yamamoto, "Deposition processes in the metallorganic chemical vapor deposition of CeO_2 films." *J. Electrochem. Soc.*, **157**, D99 (2010).
28. F. Andreatta, H. Terryn, and J. H. W. de Wit, "Corrosion behaviour of different tempers of AA7075 aluminium alloy." *Electrochim. Acta*, **49**, 2851 (2004).
29. C. M. Liao and R. P. Wei, "Galvanic coupling of model alloys to aluminum—a foundation for understanding particle-induced pitting in aluminum alloys." *Electrochim. Acta*, **45**, 881 (1999).
30. U. Tiringer, J. Kovac, and I. Milosev, "Effects of mechanical and chemical pretreatments on the morphology and composition of surfaces of aluminium alloys 7075-T6 and 2024-T3." *Corr. Sci.*, **119**, 46 (2017).
31. N. Birbilis, M. K. Cavanaugh, and R. G. Buchheit, "Electrochemical behavior and localized corrosion associated with Al_7Cu_2Fe particles in aluminum alloy 7075-T651." *Corr. Sci.*, **48**, 4202 (2006).

32. J. O. Park, C. H. Paik, Y. H. Huang, and R. C. Alkire, "Influence of Fe-Rich intermetallic inclusions on Pit initiation on aluminum alloys in aerated NaCl." *J. Electrochem. Soc.*, **146**, 517 (1999).
33. A. J. Aldykiewicz Jr, A. J. Davenport, and H. S. Isaacs, "Studies of the formation of cerium-rich protective films using X-ray absorption near-edge spectroscopy and rotating disk electrode methods." *J. Electrochem. Soc.*, **143**, 147 (1996).
34. M. Fedel, A. Ahniyaz, L. G. Ecco, and F. Deflorian, "Electrochemical investigation of the inhibition effect of CeO_2 nanoparticles on the corrosion of mild steel." *Electrochim. Acta*, **131**, 71 (2014).
35. L. G. Ecco, S. Rossi, F. Deflorian, and M. Fedel, "Electrochemical behavior of AA5005 aluminum alloy in acidic chloride-based medium containing CeO_2 nanoparticles." *J. Electrochem. Soc.*, **165**, C933 (2018).
36. L. G. Ecco, S. Rossi, F. Deflorian, and M. Fedel, "Colloidal cerium oxide nanoparticles: preparation and corrosion inhibition performance on AA5005 aluminum alloy." *J. Electrochem. Soc.*, **165**, C86 (2018).
37. J. J. Gulicovski, S. K. Milonjic, and K. Mészáros Szécsényi, "Synthesis and characterization of stable aqueous ceria sols." *Mater. Manuf. Processes*, **24**, 1080 (2009).
38. E. Matijevic, "Monodispersed metal (Hydrous) oxides—a fascinating field of colloid science." *Acc. Chem. Res.*, **14**, 22 (1981).
39. E. Matijevic, "Monodispersed colloids: art and science." *Langmuir*, **2**, 12 (1986).
40. W. P. Hsu, L. Ronnquist, and E. Matijevic, "Preparation and properties of monodispersed colloidal particles of lanthan compounds. 2. Cerium(IV)." *Langmuir*, **4**, 31 (1988).
41. E. P. Barrett, L. G. Joyner, and P. P. Halenda, "The determination of pore volume and area distribution in porous substances. I. Computations from nitrogen isotherms." *J. Am. Chem. Soc.*, **73**, 373 (1951).
42. V. Lair, L. S. Živković, O. Lupan, and A. Ringuedé, "Synthesis and characterization of electrodeposited samaria and samaria-doped ceria thin films." *Electrochim. Acta*, **56**, 4638 (2011).
43. I. Kosacki, T. Suzuki, H. U. Anderson, and P. Colomban, "Raman scattering and lattice defects in nanocrystalline CeO_2 thin films." *Solid State Ion.*, **149**, 99 (2002).
44. Z. D. Dohčević-Mitrović, M. Grujić-Brojčin, M. Šćepanović, Z. V. Popović, S. Bošković, B. Matović, M. Zinkevich, and F. Aldinger, "$Ce_{1-x}Y\ (Nd)_xO_{2-\delta}$ nanopowders: potential materials for intermediate temperature solid oxide fuel cells." *J. Phys. Condens. Matter*, **18**, S2061 (2006).
45. K. S. W. Sing, "Reporting physisorption data for gas/solid systems with special reference to the determination of surface area and porosity." *Pure Appl. Chem.*, **54**, 2201 (1982).
46. M. Pourbaix, *Atlas of Electrochemical Equilibria in Aqueous Solutions* (Pergamon, New York) (1966).
47. F. Andreatta, A. Turco, I. de Graeve, H. Terryn, J. H. W. de Wit, and L. Fedrizzi, "SKPFM and SEM study of the deposition mechanism of Zr/Ti based pre-treatment on AA6016 aluminum alloy." *Surf. Coat. Tech.*, **201**, 7668 (2007).
48. P. Visser, Y. Gonzalez-Garcia, J. M. C. Mol, and H. Terryn, "Mechanism of passive layer formation on AA2024-T3 from alkaline lithium carbonate solutions in the presence of sodium chloride corrosion science and technology." *J. Electrochem. Soc.*, **165**, C60 (2018).
49. I. Schoukens, I. Vandendael, J. De Strycker, A. A. Saleh, H. Terryn, and I. De Graeve, "Effect of surface composition and microstructure of aluminised steel on the formation of a titanium-based conversion layer." *Surf. Coat. Tech.*, **235**, 628 (2013).
50. R. Payling and T. Nelis, "Glow discharge optical emission spectroscopy: a practical guide." *RSC Analytical Spectroscopy Monographs*, ed. N. W. Barnett (The Royal Society of Chemistry, Cambridge, UK) (2003).
51. J. H. W. de Wit, "Local potential measurements with the SKPFM on aluminium alloys." *Electrochim. Acta*, **49**, 2841 (2004).
52. B. S. Tanem, G. Svenningsen, and J. Mardalen, "Relations between sample preparation and SKPFM Volta potential maps on an EN AW-6005 aluminium alloy." *Corr. Sci.*, **47**, 1506 (2005).
53. F. Andreatta, M.-E. Druart, E. Marin, D. Cossement, M.-G. Olivier, and L. Fedrizzi, "Volta potential of clad AA2024 aluminium after exposure to CeCl3 solution." *Corr. Sci.*, **86**, 189 (2014).
54. W. Melitz, J. Shena, A. C. Kummel, and S. Lee, "Kelvin probe force microscopy and its application." *Surf. Sci. Rep.*, **66**, 1 (2011).
55. P. Campestrini, H. Terryn, A. Hovestad, and J. H. W. de Wit, "Formation of a cerium-based conversion coating on AA2024: relationship with the microstructure." *Surf. Coat. Tech.*, **176**, 365 (2004).
56. A. Lanzutti, F. Andreatta, M. Magnan, and L. Fedrizzi, "Microstructural and in-depth electrochemical characterization of Zn diffusion layers on aluminum 3xxx alloy." *Surf. Interface Anal.*, **51**, 1165 (2019).
57. N. Birbilis and R. G. Buchheit, "Electrochemical characteristics of intermetallic phases in aluminum alloys: an experimental survey and discussion." *J.Electrochem. Soc.*, **152**, B140 (2005).
58. R. Ambat, A. J. Davenport, G. M. Scamans, and A. Afseth, "Effect of iron-containing intermetallic particles on the corrosion behaviour of aluminium." *Corr. Sci.*, **48**, 3455 (2006).
59. P. Schmutz and G. S. Frankel, "Characterization of AA2024-T3 by scanning Kelvin probe force microscopy." *J. Electrochem. Soc.*, **145**, 2285 (1998).
60. P. Schmutz and G. S. Frankel, "Corrosion study of AA2024-T3 by scanning Kelvin probe force microscopy and in situ atomic force microscopy scratching." *J. Electrochem. Soc.*, **145**, 2295 (1998).
61. I. Zhitomirsky and A. Petric, "Electrochemical deposition of ceria and doped ceria films." *Ceram. Int.*, **27**, 149 (2001).
62. L. S. Živković, J. P. Popić, B. V. Jegdić, Z. Dohčević-Mitrović, J. B. Bajat, and V. B. Mišković-Stanković, "Corrosion study of ceria coatings on AA6060 aluminum alloy obtained by cathodic electrodeposition: effect of deposition potential." *Surf. Coat.Tech.*, **240**, 327 (2014).
63. J. T. Dahle and Y. Arai, "Environmental geochemistry of cerium: applications and toxicology of cerium oxide nanoparticles." *Int. J. Environ. Res. Public Health*, **12**, 1253 (2015).
64. P. Borm, F. C. Klaessig, T. D. Landry, B. Moudgil, J. Pauluhn, K. Thomas, R. Trottier, and S. Wood, "Research strategies for safety evaluation of nanomaterials, part V: role of dissolution in biological fate and effects of nanoscale particle." *Toxicol. Sci.*, **90**, 23 (2006).
65. C. L. Corkhill, D. J. Bailey, F. Y. Tocino, M. C. Stennett, J. A. Miller, J. L. Provis, K. P. Travis, and N. C. Hyatt, "Role of microstructure and surface defects on the dissolution kinetics of CeO_2, a UO_2 fuel analogue." *ACS Appl. Mater. Interfaces*, **8**, 10562 (2016).
66. L. Wu, H. J. Wiesmann, A. R. Moodenbaugh, R. F. Klie, Y. Zhu, D. O. Welch, and M. Suenaga, "Oxidation state and lattice expansion of CeO_{2-x} nanoparticles as a function of particle size." *Phys. Rev. B*, **69**, 125415 (2004).